Intertwining SU(N) symmetry and frustration on a honeycomb lattice

Xu-Ping Yao,* Rui Leonard Luo,* and Gang Chen†

Department of Physics and HKU-UCAS Joint Institute for Theoretical and Computational Physics at Hong Kong, The University of Hong Kong, Hong Kong, China

(Received 7 November 2021; revised 18 December 2021; accepted 20 December 2021; published 3 January 2022)

Large symmetry groups in quantum many-body systems could strongly enhance quantum fluctuations and thereby stabilize exotic quantum phases. Frustrated interactions were long known to have similar effects. Here we intertwine the large SU(N) symmetry and the frustration in a J_1-J_2 SU(N) Heisenberg model on a honeycomb lattice, where J_1 is the nearest-neighbor coupling and J_2 is the next-nearest-neighbor coupling. With a large-N analysis, we obtain a rich phase diagram by varying both N and the ratio J_2/J_1. The ground states include Dirac spin liquid, chiral spin liquid, valence cluster solids, flux ordered state, and stripe states. The physical properties of each phase are discussed.

DOI: 10.1103/PhysRevB.105.024401

I. INTRODUCTION

In quantum many-body systems with a large symmetry group, the quantum fluctuations can be intensively enhanced and thus prevent the formation of the conventional orders. Therefore, the large symmetry group provides an interesting direction to stabilize novel and exotic quantum states. This scenario is fundamentally different from the common classical limit with a large spin moment in most solid-state magnets where a large local Hilbert space is also encountered. Over there, the model Hamiltonian does not have nor is proximate to a large symmetry group to access the large local Hilbert space effectively to enhance the quantum fluctuations. Therefore, having or being proximate to a large symmetry group can be one important ingredient to realize exotic quantum phases. In condensed matter physics, the large symmetry group is often considered as a theoretical fantasy to access exotic quantum phases and limits [1–3].

Now several realistic quantum many-body systems may turn this theoretical fantasy into reality. As a representative, the ultracold-atom system has been substantially developed to achieve the large symmetry like the SU(N) symmetries in the fermionic cold gases, especially alkaline-earth atoms (AEAs) [4–8]. The past few years have witnessed the reports of many nontrivial phenomena in this platform including Mott crossover, antiferromagnetic spin correlation, bosonization of the SU(N) fermions, Pomeranchuk effects, and pronounced interaction effects [5,9–14]. Quite recently, the highly tunable two-dimensional (2D) moiré materials have been proposed to be a new candidate where the Hubbard models with SU(4) and SU(8) symmetries can be realized through meticulously designed stacking and twisting [15–17].

In this rapidly evolving field, the SU(N) Mott insulators have attracted significant attention because they are a straightforward generalization of the conventional SU(2) one. Tremendous efforts have been made on the theoretical side to reveal their nature and it turns out that various interesting ground states could emerge depending not only on the lattice and the number N but also on the filling per site [12,18–27]. Although the SU(N) symmetry seems to be more like an idealization in the realistic solid-state materials than the ultracold-atom systems, the Hubbard model with emergent SU(4) symmetry has been proposed to capture the effective physics of the spin-orbital compounds such as the Kugel-Khomskii spin-orbital system $Ba_3CuSb_2O_9$ [28] and the spin-orbit-entangled system α-$ZrCl_3$ [29,30], and even on the moiré superlattice such as twisted bilayer graphene and transition metal dichalcogenides [15–17].

In particular, the SU(N) spin physics on the honeycomb lattice with only the nearest-neighbor antiferromagnetic Heisenberg interactions has been extensively studied from

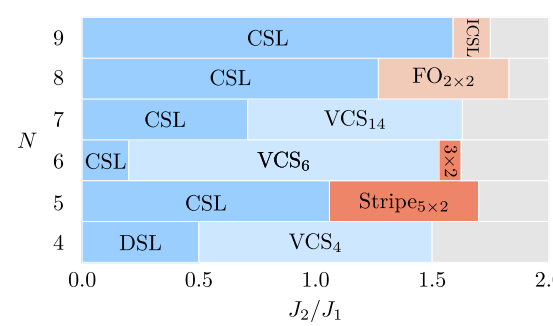

FIG. 1. Phase diagram for the SU(N) spins ($4 \leqslant N \leqslant 9$) with J_1-J_2 Heisenberg interactions on the honeycomb lattice. The CSL and inhomogeneous chiral spin liquid (ICSL) states have total flux $4\pi/N$ and $2\pi/N$ through the unit cell, respectively. The subscripts for valence cluster solids (VCSs) represent the numbers of sites in each cluster. The subscripts for stripe and flux ordered (FO) states indicate the periods of the enlarged unit cells. In the gray regions, the system is decoupled into two equivalent triangular subsystems.

*These authors contributed equally to this work.
†gangchen@hku.hk

 ©2022 American Physical Society

both theoretical and numerical perspectives. For the SU(2) spins, the system is unfrustrated due to the bipartiteness of the lattice and the ground state has an antiferromagnetic Néel order. A valence bond state with the hexagonal plaquettes is found for the SU(3) spins by tensor network simulations and further confirmed by exact diagonalizations and variational Monte Carlo studies [31–33]. The SU(4) case is the most attractive because it is believed to support a peculiar spin liquid state known as the U(1) Dirac spin liquid (DSL) [34]. In contrast, the $N = 5$ case is less studied. The ground states of SU($N \geqslant 6$) spins are inferred to be chiral spin liquid (CSL) states [18,35,36] albeit the SU(6) case is still under debate [37].

Another important but more well-known ingredient to stabilize exotic quantum phases is the magnetic frustration [38]. For the honeycomb lattice that is discussed here, the introduction of the next-nearest-neighbor Heisenberg interactions would frustrate the antiferromagnetic Néel ground state of the nearest-neighbor SU(2) Heisenberg interaction. Even at the classical level, it has been shown that a spiral spin liquid regime could emerge from the Néel-ordered state in the large-S (classical) limit where quantum fluctuations are suppressed [39,40]. For the spin-1/2 quantum case, the density matrix renormalization group calculation suggests a deconfined quantum phase transition from the Néel order to the plaquette order [41].

In this work, we plan to explore the interesting situation where both the large symmetry group and frustration are present in one system, and examine the consequences by intertwining these two ingredients. The SU(N) honeycomb lattice J_1-J_2 spin model is a manifestation of this intertwining. Despite the existing results on the nearest-neighbor SU(N) honeycomb lattice spin model, the role of the next-nearest-neighbor interactions for general SU(N) spins with enhanced quantum fluctuations is not yet clear except for $N \leqslant 3$ [42–45]. Moreover, the low-energy physics of the U(1) DSL for the SU(4) spins is effectively captured by a compact QED_3 theory with $N_f = 8$ Dirac fermions coupled to a dynamic U(1) gauge field [46]. It is generally believed that the large number of gapless matter could stabilize the U(1) DSL by suppressing the space-time monopole events. It is, however, still unclear about the lower bound for the critical number of the gapless matter modes for this stabilization [47,48]. Since the U(1) DSL is expected to be the parent state of many competing states in two dimensions by the spontaneous generation of the Dirac masses [49], it would be interesting to explore the nearby (descending) phases with the SU(N) spin systems. Therefore, the fate of the U(1) DSL with further interactions has triggered growing research interests [50–53]. We attempt to fill the gap at the mean-field level by investigating the SU($4 \leqslant N \leqslant 9$) Heisenberg model on the honeycomb lattice with both nearest-neighbor and next-nearest-neighbor antiferromagnetic interactions. Given that the decoupled limit where the system reduces to the triangular antiferromagnetic model has been explored in our previous work [20], we focus on the finite next-nearest-neighbor interactions here and construct the phase diagram in the large-N approximation. The mean-field results are summarized in Fig. 1. Our results confirm the existence of the putative DSL state for SU(4) spins and the CSL states for larger parameter N. It is found that both of them have a uniform background U(1) gauge flux $4\pi/N$ piercing the hexagonal plaquettes and remain stable against the weak next-nearest-neighbor interactions. When the next-nearest-neighbor interactions become stronger but have not driven the system into the decoupled regime, a plethora of intermediate quantum states emerge for different parameter N, including the inhomogeneous chiral spin liquids (ICSLs), valence cluster solids (VCSs), and stripe and flux ordered (FO) states. All these intermediate quantum states break various lattice translational symmetries. The richness of the phase diagram reveals the intense competition of the low-energy states due to the quantum fluctuation and frustration.

The rest of the paper is organized as follows. The SU(N) Hubbard model and the derivative SU(N) Heisenberg Hamiltonian in the strong-coupling limit are introduced in Sec. II. With the representation of the constrained fermions, a mean-field Hamiltonian is obtained in the large-N limit, whose parameters are defined by the saddle-point equations. Then a self-consistent minimization algorithm is employed to solve the saddle-point equations and find the ground states of the mean-field Hamiltonian strictly satisfying the local constraints. Specifically, the DSL and the descending tetramer states for the SU(4) spins are discussed in Sec. III. The CSL and other intermediate quantum phases for higher SU(N) spins are described in Sec. IV. The paper is concluded in Sec. V.

II. LARGE-N APPROXIMATION OF SU(N) HEISENBERG MODEL

The SU(N) Hubbard model at $1/N$ filling (or equivalently with one particle per site) can be reduced to the Heisenberg model of SU(N) spins in the strong-coupling limit up to second order. The effective spin with an internal SU(N) symmetry is naturally introduced at each lattice site and can be expressed with the N-flavor Abrikosov fermions as $S_{\alpha\beta}(\boldsymbol{r}) = f^\dagger_{\boldsymbol{r}\alpha} f_{\boldsymbol{r}\beta}$, where $\alpha, \beta = 1, \ldots, N$. This fundamental representation is accompanied by a local constraint on the fermions $f^\dagger_{\boldsymbol{r}\alpha} f_{\boldsymbol{r}\alpha} = 1$ to reduce the enlarged Hilbert space. Note that a summation over repeated flavor indices is supposed hereafter unless otherwise specified. We consider such an SU(N) Heisenberg model on the honeycomb lattice,

$$\mathcal{H} = J_1 \sum_{\langle \boldsymbol{r}\boldsymbol{r}' \rangle} S_{\alpha\beta}(\boldsymbol{r}) S_{\beta\alpha}(\boldsymbol{r}') + J_2 \sum_{\langle\langle \boldsymbol{r}\boldsymbol{r}' \rangle\rangle} S_{\alpha\beta}(\boldsymbol{r}) S_{\beta\alpha}(\boldsymbol{r}'), \quad (1)$$

where both the nearest-neighbor and next-nearest-neighbor exchange interactions $J_{1,2}$ are antiferromagnetic. It is apparent that in the $J_2/J_1 \to \infty$ limit, this model is equivalent to two decoupled SU(N) Heisenberg models on triangular sublattices that have been studied in our previous work and others [20,54–56]. Here we still employ the large-N saddle-point approximation to explore the nature in the moderate J_2/J_1 regime for different SU(N) spins. Distinct from a perturbative expansion in the size of the interactions, this method has the advantages of preserving the spin symmetry and controlling systematic error by the higher-order correction in $1/N$ [3,19]. The partition function of the spin Hamiltonian in Eq. (1) can be expressed in the form of an imaginary-time functional

integral:

$$\mathcal{Z} = \int \mathcal{D}\chi^\dagger \mathcal{D}\chi \mathcal{D}\mu \mathcal{D}f^\dagger \mathcal{D}f e^{-\mathcal{S}}. \tag{2}$$

The action is given as

$$\mathcal{S} = \int_0^\beta d\tau \Big\{ \sum_{\boldsymbol{r}} f_{\boldsymbol{r}\alpha}^\dagger \partial_\tau f_{\boldsymbol{r}\alpha} + \mu_{\boldsymbol{r}}(f_{\boldsymbol{r}\alpha}^\dagger f_{\boldsymbol{r}\alpha} - 1) + \sum_{\langle \boldsymbol{r}\boldsymbol{r}'\rangle, \langle\langle \boldsymbol{r}\boldsymbol{r}'\rangle\rangle} (\chi_{\boldsymbol{r}\boldsymbol{r}'} f_{\boldsymbol{r}\alpha}^\dagger f_{\boldsymbol{r}'\alpha} + \text{H.c.}) + \frac{N}{\mathcal{J}_{\boldsymbol{r}\boldsymbol{r}'}} |\chi_{\boldsymbol{r}\boldsymbol{r}'}|^2 \Big\}. \tag{3}$$

A set of Lagrange multipliers $\mu_{\boldsymbol{r}}$ has been introduced to enforce the single occupation constraint on each lattice site. There are also two types of auxiliary fields $\chi_{\boldsymbol{r}\boldsymbol{r}'}$ for the nearest-neighbor and next-nearest-neighbor bonds, to decouple the fermion operators. For the sake of simplicity, we have redefined the exchange couplings as $\mathcal{J}_{\langle \boldsymbol{r}\boldsymbol{r}'\rangle} = NJ_1 = 1$ and $\mathcal{J}_{\langle\langle \boldsymbol{r}\boldsymbol{r}'\rangle\rangle} = NJ_2 = J_2/J_1$. Taking the large-$N$ limit on the action $\mathcal{S}$ leads to the mean-field Hamiltonian for the noninteracting fermionic spinons,

$$\mathcal{H}_{\text{MF}} = \sum_{\langle \boldsymbol{r}\boldsymbol{r}'\rangle, \langle\langle \boldsymbol{r}\boldsymbol{r}'\rangle\rangle} \frac{N}{\mathcal{J}_{\boldsymbol{r}\boldsymbol{r}'}} |\chi_{\boldsymbol{r}\boldsymbol{r}'}|^2 + (\chi_{\boldsymbol{r}\boldsymbol{r}'} f_{\boldsymbol{r}\alpha}^\dagger f_{\boldsymbol{r}'\alpha} + \text{H.c.}) + \sum_{\boldsymbol{r}} \mu_{\boldsymbol{r}}(1 - f_{\boldsymbol{r}\alpha}^\dagger f_{\boldsymbol{r}\alpha}), \tag{4}$$

and the saddle-point equations

$$\langle f_{\boldsymbol{r}\alpha}^\dagger f_{\boldsymbol{r}\alpha}\rangle = 1, \tag{5}$$

$$\chi_{\langle \boldsymbol{r}\boldsymbol{r}'\rangle} = -\langle f_{\boldsymbol{r}'\alpha}^\dagger f_{\boldsymbol{r}\alpha}\rangle/N, \tag{6}$$

$$\chi_{\langle\langle \boldsymbol{r},\boldsymbol{r}'\rangle\rangle} = -J_2/J_1 \langle f_{\boldsymbol{r}'\alpha}^\dagger f_{\boldsymbol{r}\alpha}\rangle/N. \tag{7}$$

In the following sections, we determine the ground-state phase diagram of the spinon mean-field Hamiltonian in Eq. (4) with $2 \leqslant N \leqslant 9$ numerically by utilizing the self-consistent minimization (SCM) algorithm developed in Refs. [18,19]. We extend this algorithm in order to involve the antiferromagnetic next-nearest-neighbor interactions by treating the two types of auxiliary fields $\chi_{\boldsymbol{r}\boldsymbol{r}'}$ on the honeycomb lattice and triangular sublattices synchronously and updating the chemical potentials $\mu_{\boldsymbol{r}}$ unitedly. The rest of the technical details are briefly described in the Appendix. It should be emphasized that, differing from the usual analytical method where the local constraints are enforced only on average, the numerical SCM algorithm faithfully respects the single occupation constraints on each lattice site [19]. Therefore, the obtained results are very reliable at the mean-field level, especially when the systematic correction beyond the mean-field results becomes negligible with increasing the flavor number N.

III. MEAN-FIELD RESULTS FOR $N \leqslant 4$

The implementation of the SCM algorithm needs *a priori* knowledge of the periodic structure of possible ground states. The results after optimization are sometimes sensitive to the chosen lattice geometry, especially for the cluster states that have large unit cells and break the lattice symmetries. To accommodate different candidate ground states as much as possible, the two-site unit cell of the primitive honeycomb lattice is enlarged along two directions of its lattice vectors by factors ℓ_1 and ℓ_2, respectively. We then consider all enlarged unit cells with the parallelogram geometries $\ell_{1,2} \leqslant N$ with periodic boundary conditions. In our calculation, the SCM algorithm is not used to handle arbitrary fillings currently on a certain unit cell geometry; the number of fermions per cell is set to be an integer and equal to $2\ell_1\ell_2/N$. Geometries that do not meet this condition or have any unit width $\ell_{1,2} = 1$ are excluded. Meanwhile the reduced Brillouin zone is discretized into an $L_1 \times L_2$ mesh with $L_{1,2} = 50$ for $2 \leqslant N \leqslant 6$ and $L_{1,2} = 20$ for $7 \leqslant N \leqslant 9$. For a given J_2/J_1 and each allowed geometry, the SCM algorithm is run at least 64 times with different random seeds to reach the best optimized saddle-point energy which is accepted as the global minimum. The results are discussed in the following and the ground-state phase diagram for $4 \leqslant N \leqslant 9$ is presented in Fig. 1.

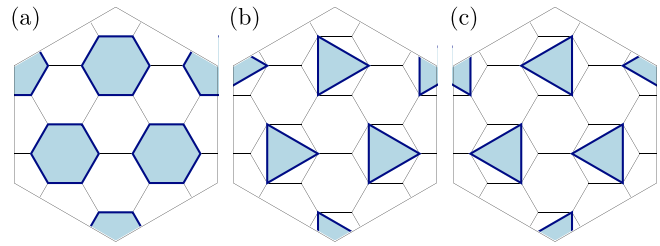

FIG. 2. The VCS states for the SU(3) spins. (a) An ordered hexagonal pattern form on the nearest-neighbor bonds coexisting with (b, c) the three-site simplex VCS patterns on the next-nearest-neighbor bonds. The expectation values $\chi_{\langle \boldsymbol{r}\boldsymbol{r}'\rangle}$ decrease with the increasing nearest-neighbor exchange interaction and eventually vanish at $J_2/J_1 = 0.50$.

We first discuss the numerical results for the SU(2) and SU(3) spins as a comparison. For $N < 4$, the parameter N is not quite a large parameter yet. Therefore, the large-N approximation may give incorrect ground states, and this is what happened in our study of the triangular lattice where the actual ground state of the SU(2) Heisenberg model is the 120° order [20]. This statement, however, strongly depends on the underlying system. For the J_1-J_2 Heisenberg model on the honeycomb lattice, we find the ground state for the SU(2) spins is highly degenerate and is given by any dimer covering state on the nearest-neighbor bonds in the range $0.0 \leqslant J_2/J_1 \leqslant 0.5$, and the expectation values of the next-nearest-neighbor bonds are exactly zero. When $J_2/J_1 \geqslant 0.5$, the ground state is given by any dimer covering state on the next-nearest-neighbor bonds, and the expectation values of nearest-neighbor bonds are exactly zero. This is certainly a significant deviation from the actual ground states. Nevertheless, the SCM algorithm reproduces the hexagonal plaquette VCS state correctly for the SU(3) spins at $J_2/J_1 = 0$ as shown in Fig. 2(a). It is found that the finite interaction J_2 induces nonvanishing bond expectations $\chi_{\langle\langle \boldsymbol{r}\boldsymbol{r}\rangle\rangle}$ that form the three-site simplex VCS on two triangular sublattices illustrated in Figs. 2(b) and 2(c). The hexagonal VCS order coexists with the three-site simplex VCS order up to $J_2/J_1 = 0.5$ and then the system smoothly enters into the decoupled limit where $\chi_{\langle \boldsymbol{r}\boldsymbol{r}'\rangle} = 0$. It is worth noting that the three-site simplex VCS state is still not the true ground state for the SU(3) spins on

the decoupled triangular sublattice [57]. It is expected that the mean-field ground states in the large-N approximation become more reliable when the systematic error is suppressed more for $N > 3$.

A. Dirac spin liquid and its instability to tetramerization

For the SU(2) antiferromagnetic Heisenberg model on the honeycomb lattice, there could be a Dirac node of the spinon bands without any flux at the mean-field level. Another DSL state has also been proposed for the SU(4) spins where the spinon filling is at 1/4 [34] and the mean-field theory is characterized by

$$\chi_{\langle \boldsymbol{rr}'\rangle} = |\chi_1| e^{\imath a_{\langle \boldsymbol{rr}'\rangle}}, \tag{8}$$

$$\sum_{\boldsymbol{rr}'\in \mathrm{hex}} a_{\boldsymbol{rr}'} = \pi, \tag{9}$$

$$\mu_{\boldsymbol{r}} = 0. \tag{10}$$

All the nearest-neighbor bonds have a uniform expectation value $|\chi_1|$ but are modulated by a U(1) gauge field $a_{\langle \boldsymbol{rr}'\rangle}$ such that the gauge flux is equal to π per hexagon. This is confirmed by our calculation. It is further found that such a π-flux DSL state is stable against the presence of the next-nearest-neighbor interactions until $J_2/J_1 \approx 0.50$. Specifically, the mean-field saddle point gives a compatible gauge flux pattern on the triangular sublattices as

$$\chi_{\langle\langle \boldsymbol{rr}'\rangle\rangle} = |\chi_2| e^{\imath a_{\langle\langle \boldsymbol{rr}'\rangle\rangle}}, \tag{11}$$

$$\sum_{\boldsymbol{rr}'\in \mathrm{tri}} a_{\boldsymbol{rr}'} = 0 \text{ or } \pi, \tag{12}$$

where $|\chi_2|$ is dependent on J_2/J_1 and different from $|\chi_1|$. The gauge choice $a_{\langle\langle \boldsymbol{rr}'\rangle\rangle}$ on the two types of sublattices is not independent once the one on the nearest-neighbor bonds is fixed. In Figs. 3(a)–3(c), we illustrate the mean-field ansatz refined from our numerical results. It turns out that there is a staggered flux of zero and π on each sublattice, which is nothing but the ansatz of the DSL state on the triangular lattice [58]. Consequently, the Dirac nodes are intact as the $J_2/J_1 = 0$ case except for the energy shifts. In the reduced Brillouin zone [see Fig. 3(d)], we plot the spinon band structure around the center $\bar{\Gamma}$. The Dirac touchings occur at $\bar{\Gamma}$ and $\bar{K}$ ($\bar{K}'$) points for the quarter and half fillings [see Fig. 3(e)].

With the increasing of the next-nearest-neighbor interactions, a four-site VCS state prevails over the DSL state before the decoupled limit at $J_2/J_1 = 1.5$. The spinons tetramerize as an SU(4) singlet on four adjoining sites as sketched in Fig. 4(a). Such a tetramerization was also obtained by the variational Monte Carlo approach [59]. There are two nonequivalent but symmetry-related tetramers within the 2×2 enlarged unit cell. At the same time, a three-site simplex VCS forms on the next-nearest-neighbor bonds around each center of the tetramers, leaving the center site dangling. In the decoupled limit, the dangling site is also incorporated to form the SU(4) singlet on the triangular sublattice. Here, the four-site VCS state is accompanied by a large degeneracy in the large-N limit, because any covering of the tetramers has the same energy. Only one type of covering of the tetramers is demonstrated here.

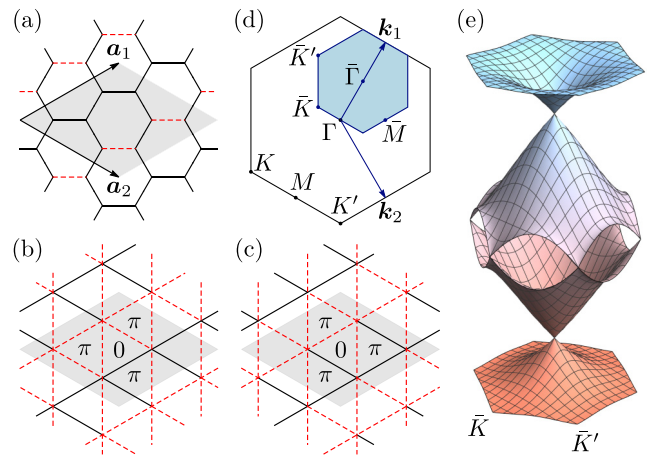

FIG. 3. The Dirac spin liquid for the SU(4) spins. The gauge choice implements (a) π flux on each hexagonal plaquette formed by the nearest-neighbor bonds and (b, c) staggered $0/\pi$ flux on the triangular plaquettes formed by the next-nearest-neighbor bonds. The hopping amplitudes are positive on the solid black bonds and negative on the dashed red bonds. The gray diamonds indicate the same enlarged unit cell containing eight sites. (d) The original (outermost) and reduced (blue hexagon) Brillouin zones and the high-symmetry momenta. (e) The twofold-degenerate spinon spectrum within the reduced Brillouin zone for the Dirac spin liquid here.

B. Fidelity susceptibility

To confirm the stability of the π-flux DSL state, we further apply the exact diagonalization (ED) method [60] to different geometries of the enlarged unit cell and calculate the ground-state fidelity metric [61] as a function of the next-nearest-neighbor interaction J_2,

$$g = \frac{2}{N_s} \frac{1 - |\langle \psi(J_2)|\psi(J_2 + \delta J_2)\rangle|}{(\delta J_2)^2}. \tag{13}$$

As only one parameter is varied, this entry of fidelity metric is known as fidelity susceptibility. Here the ground-state wave function ψ is obtained by the ED method and N_s is the number of sites within the supercell. The fidelity $|\langle \psi(J_2)|\psi(J_2 + \delta J_2)\rangle|$ measures the orthogonality between

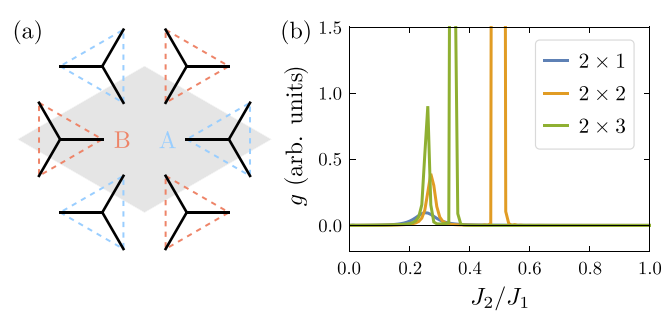

FIG. 4. (a) The ordered singlet tetramers (solid) for SU(4) spins on the nearest-neighbor bonds and two types of three-site simplex VCSs (dashed and colored) around the center of the tetramer on the next-nearest-neighbor bonds. The gray diamond indicates the enlarged unit cell. (b) The fidelity metric g as a function of J_2/J_1 for different supercells.

two ground states that are infinitesimally close to each other in the J_2 space. The fidelity tends to vanish when there is a symmetry-breaking or topological phase transition and thus results in a visible peak for the quantity g. The latter has been treated as a sensitive indicator of Mott transition for the SU(N) Hubbard model [22].

As shown in Fig. 4(b), we implement the fidelity calculations on supercells with the geometries of 2×1, 2×2, and 2×3. The number of sites $N_s = 4$, 8, and 12 respectively. For all geometries, there is a fairly consistent peak at $J_2/J_1 \approx 0.26$ that becomes sharper with the increasing of system size. It could be an evidence for the persistence of the DSL state, although the critical value J_2/J_1 is about half of the mean-field result. There seems to be another phase transition for larger J_2/J_1 but no consistent results for geometries considered here. In fact, the potential four-site VCS state is incompatible with the lattice geometries that contain an odd width. The failure implies that the finite-size effect is still prominent for the stronger next-nearest-neighbor interactions.

IV. MEAN-FIELD RESULTS FOR $5 \leqslant N \leqslant 9$

Going beyond $N = 4$, the expanding symmetry group stimulates the quantum fluctuations effectively and favors nonmagnetic states with a huge classical degeneracy. This is believed to be present on any lattice for large enough N. On the honeycomb lattice, the magnetic frustration is incorporated by the next-nearest-neighbor Heisenberg interactions for the case of the SU(2) spins. The classical degeneracy may be significantly augmented, resulting in novel quantum states. Nevertheless, peculiar quantum-ordered states could also be stabilized due to the competition between the geometric frustration and the structure of the large SU(N) symmetry. The synergism and antagonism of the two ingredients are further explored for the large-N regime in this section.

A. Chiral spin liquid for $5 \leqslant N \leqslant 9$

The putative CSL states for SU($N > 4$) spins are confirmed in our mean-field calculations and are quite stable against the next-nearest-neighbor interactions especially for larger N as shown in Fig. 1. The fall of the CSL states occurs at $J_2/J_1 \approx 1.06$, 0.20, 0.71, 1.27, and 1.59 for $5 \leqslant N \leqslant 9$, respectively. This CSL state preserves all lattice translational symmetries but breaks the time-reversal and parity symmetries spontaneously through the following mean-field ansatz on the nearest-neighbor bonds,

$$\chi_{\langle \boldsymbol{rr'} \rangle} = |\chi_1| e^{\imath a_{\langle \boldsymbol{rr'} \rangle}}, \tag{14}$$

$$\sum_{\boldsymbol{rr'} \in \text{hex}} a_{\boldsymbol{rr'}} = \frac{4\pi}{N}, \tag{15}$$

$$\mu_{\boldsymbol{r}} = 0, \tag{16}$$

and on the next-nearest-neighbor bonds,

$$\chi_{\langle\langle \boldsymbol{rr'} \rangle\rangle} = |\chi_2| e^{\imath a_{\langle\langle \boldsymbol{rr'} \rangle\rangle}}, \tag{17}$$

$$\sum_{\boldsymbol{rr'} \in \text{A;tri}} a_{\boldsymbol{rr'}} = \sum_{\boldsymbol{rr'} \in \text{B;tri}} a_{\boldsymbol{rr'}} = \frac{4\pi}{N} + \phi, \tag{18}$$

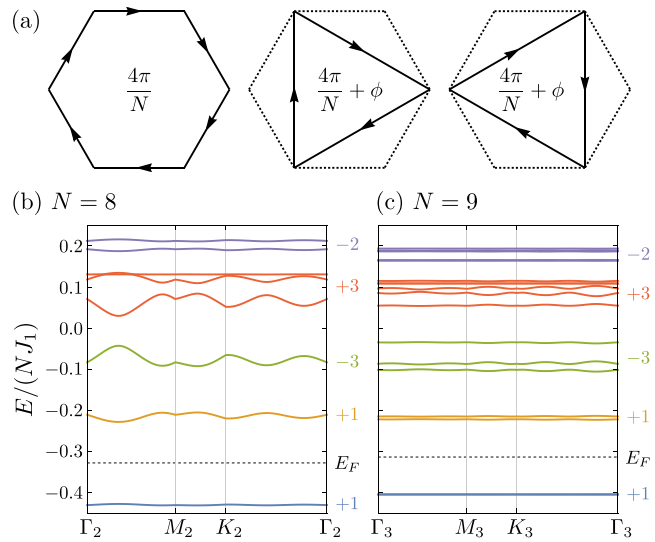

FIG. 5. (a) The CSL states for $5 \leqslant N \leqslant 9$ resemble the Haldane model with a total flux $4\pi/N$ through the unit cell. The gauge fluxes per hexagonal and triangular plaquettes are indicated by arrows where ϕ is only dependent on J_2. (b, c) The spinon spectra for CSL states with $N = 8$ and 9 at $J_2/J_1 = 0.5$. The spinon bands are grouped in colors according to their separations and labeled with their total first Chern numbers. High-symmetry momenta with the subscript ℓ are defined in the reduced hexagonal Brillouin zones for $\ell \times \ell$ enlarged unit cells.

where the U(1) gauge fields $a_{\boldsymbol{rr'}}$ and the corresponding gauge fluxes per hexagonal and triangular plaquettes are indicated by arrows in Fig. 5(a). The letters A and B label two types of triangular sublattices, and the U(1) flux difference ϕ is dependent on J_2 for a given N. It is obvious that such a mean-field solution resembles the well-known Haldane model [62] for the quantum anomalous Hall effect despite that the total flux through the unit cell is quantized to $4\pi/N$ instead of zero. For even parameters N (half-integer spins), the CSL state has a spinon spectrum with N bands where only the lowest one is fully occupied. On the other hand, there are $2N$ bands for odd parameter N (integer spins) and the lowest two are fully filled by the spinons. In Figs. 5(b) and 5(c), we plot such spinon band structures or the CSL states with $N = 8$ and 9 in their reduced Brillouin zones. The corresponding unit cells are enlarged by 2×2 and 3×3, respectively. Therefore, the reduced Brillouin zones are still hexagons and the high-symmetry momenta are defined similarly as in Fig. 3(d). For simplicity, we distinguish them by the subscript ℓ for an $\ell \times \ell$ enlarged unit cell hereafter. For both even and odd parameters N, there is a finite energy gap between occupied spinon bands and others with higher energies due to the U(1) gauge pattern, which means the absence of the spinon Fermi surface. Since the spinon bands are not well separated from each other in general, the associated first Chern number is generalized to

$$C_1 = \frac{1}{2\pi} \int_{\text{BZ}} d\boldsymbol{k} \text{Tr}[\mathcal{F}_{ij}(\boldsymbol{k})], \tag{19}$$

where the non-Abelian Berry curvature $\mathcal{F}_{ij} = \partial_i \mathcal{A}_j - \partial_j \mathcal{A}_i - \imath[\mathcal{A}_i, \mathcal{A}_j]$ is written in terms of the matrix-valued Berry connection $\mathcal{A}_i$ that has the elements $[\mathcal{A}_i]^{nm} = \imath \langle \psi_n | \partial_i | \psi_m \rangle$ [63].

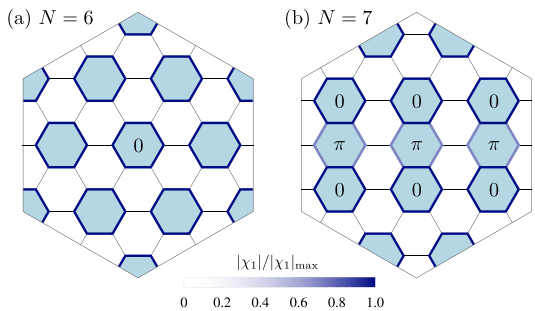

FIG. 6. (a) The six-site VCS state for the SU(6) spins. (b) The 14-site VCS state for the SU(7) spins. The bond expectation values $|\chi_1|$ are colored with respect to their relative magnitudes in each case. The shaded plaquettes enclose zero or π flux as indicated. J_2/J_1 is taken to be 1.00.

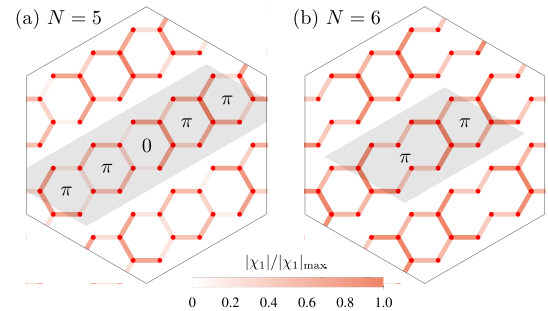

FIG. 7. Stripe state with (a) a 5×2 enlarged unit cell for SU(5) spins and (b) a 3×2 enlarged unit cell for SU(6) spins. Dashed quadrilaterals indicate the enlarged unit cell. The bond expectation values $|\chi_1|$ are colored with respect to their relative magnitudes in each case. Some regions enclose zero or π flux as indicated. J_2/J_1 is taken to be 1.60.

Here (k_i, k_j) is the momentum in the Brillouin zone and $\partial_i = \partial/\partial_{k_i}$. The trace is taken over the eigenstates denoted as $\psi_n(\boldsymbol{k})$ for the nth energy level. In Figs. 5(b) and 5(c), the spinon bands are also grouped according to the separations and labeled with their total first Chern numbers. It turns out that the occupied spinon bands possess the first Chern number $C_1 = \pm 1$ (the sign is determined by the chirality of the U(1) gauge flux). This is a universal result of the CSL phase with different parameters N and interactions. Therefore, this gapped system exhibits a nonzero Hall conductivity $\sigma_{xy} = N/2\pi$ after counting contributions from all N spin flavors. By integrating the gapped spinon out, one can further obtain a Chern-Simons term in the action

$$\mathcal{S}_{\mathrm{CS}} = \frac{N}{4\pi} \int dt d\boldsymbol{r} \epsilon_{\mu\nu\lambda} a_\mu \partial_\nu a_\lambda, \tag{20}$$

describing the dynamics of U(1) gauge field in $2+1$ dimensions and in the continuum limit. It is the Chern-Simons term that determines the topological properties of the CSL state. In fact, it endows the spinon with an attached flux $2\pi - 2\pi/N$ and renders the fractional statistics to the excitations known as anyons. For CSL states found here, the low-energy physics of the U(1) gauge fluctuation can be captured by a topological quantum field theory containing anyons with a statistical angle $\pi \pm \pi/N$. With open boundaries, there are also gapless chiral modes with the spin degrees of freedom propagating along the edges of the system, which are described by the chiral $\mathrm{SU}(N)_1$ Wess-Zumino-Witten (WZW) model.

B. Valence cluster solid and stripe states

In general, the formation of an SU(N) singlet requires at least N spins. These multisite singlets may be rapidly transformed into each other due to the SU(N) exchanges. Nevertheless, as shown in Fig. 1, two stable VCS states are identified for $N = 6$ and 7 in the regimes $0.20 \lesssim J_2/J_1 \lesssim 1.53$ and $0.71 \lesssim J_2/J_1 \lesssim 1.63$, respectively. In Fig. 6, we present two such VCS states and color the nearest-neighbor bond expectation values $|\chi_1|$ with respect to their relative magnitudes. For SU(6) spins, the singlet contains six spins and manifests as a hexagon plaquette with a uniform $|\chi_1|$ and zero flux. This is reminiscent of the same structure proposed for SU(3) spins depicted in Fig. 2(a). The SU(7) case is more complicated. A 14-site cluster is formed on the nearest-neighbor bonds through two different expectation values and ordered with long periods as shown in Fig. 6(b). Note that the center hexagon with four weak bond magnitudes encloses π flux.

For the SU(5) and SU(6) spins, the intermediate quantum states manifest as stripe orders in the regimes $1.07 \lesssim J_2/J_1 \lesssim 1.70$ and $1.53 \lesssim J_2/J_1 \lesssim 1.63$, respectively. In Fig. 7 we illustrate these stripe states on the nearest-neighbor bonds at $J_2/J_1 = 1.60$. It can be found that the inhomogeneous expectation values on the nearest-neighbor bonds lead to a enlarged unit cell containing 20 (12) sites for the $N = 5$ ($N = 6$) case. Both cases have a doubling to one of the primitive honeycomb lattice vectors. Along this direction, the bond expectation values vanish alternatively and result in a noncontact stripe pattern. This doubling is consistent with the adjacent stripe state of SU(5) spins in the decoupled limit [20]. Along the other direction, the enhanced periodicities are quintuple (triple) for the $N = 5$ ($N = 6$) case. Some regions enclose zero or π flux as indicated in Fig. 7, but the total flux within the enlarged unit cell is still zero and thus the time-reversal symmetry is preserved. The stripe states are also extensively degenerate; several different distributions of bond expectation values are found by the SCM algorithm and they have the exact same stripe pattern including the flux ordering. Likewise, the degeneracy is expected to be lifted upon incorporating perturbative $1/N$ corrections.

C. Flux ordered state for $N = 8$

Apart from the VCS and stripe states, an intermediate state breaking the lattice translational symmetries is found for SU(8) spins in the range $1.27 \lesssim J_2/J_1 \lesssim 1.83$. There is a period doubling along both directions of the primitive honeycomb lattice vectors. Within the 2×2 enlarged unit cell, the U(1) gauge fluxes per hexagonal and triangular plaquettes are always zero or π and ordered in a pattern shown in Fig. 8(a). Thus, the lattice translation symmetry is explicitly broken. Hence we refer to it as the flux ordered state. The time-reversal symmetry is preserved here, and the CSL state does not apply here. The spinon band structure consists of eight twofold-degenerate bands where the lowest one is fully filled and all others are empty. To preserve the point

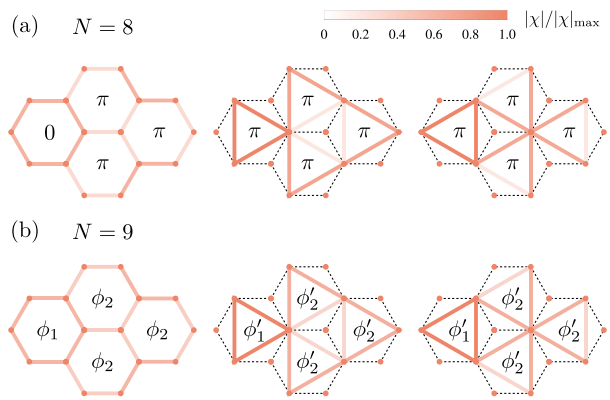

FIG. 8. (a) The FO state with a 2×2 enlarged unit cell for $N = 8$ at $J_2/J_1 = 1.50$. The gauge fluxes are constantly fixed to zero or π. (b) The ICSL state for $N = 9$ at $J_2/J_1 = 1.70$. This state also has a 2×2 enlarged unit cell. The total flux on four hexagonal plaquettes is $\phi_1 + 3\phi_2 = 2\pi/9$. The two fluxes on triangular plaquettes within the same hexagon satisfy the similar relationship as the CSL state. The bond expectations are colored with respect to their relative magnitudes in each case.

symmetries of the underlying honeycomb lattice, we take a supercell with the 4×4 geometry and present the spinon band structure in the reduced Brillouin zone as shown in Fig. 9(a). Here, each band possesses a fourfold degeneracy due to the extra unit cell doubling. Although the eight groups of spinon bands are well separated from each other, their first Chern number vanishes due to the time-reversal symmetry. As the spinon in this flux ordered state is fully gapped, the spinon deconfinement is unstable to the U(1) gauge fluctuation, and the system will become confined. The system would behave more like a confined valence cluster state.

D. Inhomogeneous chiral spin liquid for $N = 9$

Interestingly, there exists another type of CSL state for the SU(9) spins in the narrow range $1.59 \lesssim J_2/J_1 \lesssim 1.75$.

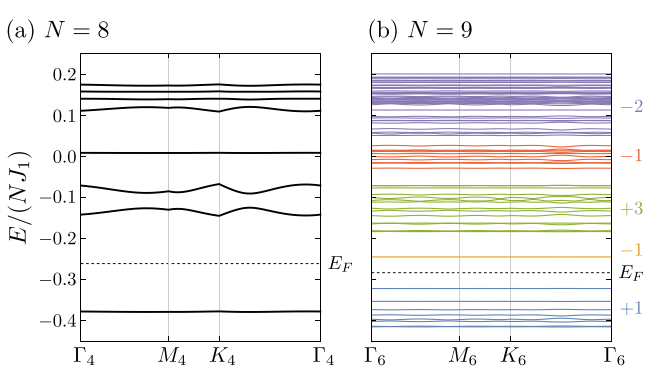

FIG. 9. (a) Spinon spectrum for the FO state at $J_2/J_1 = 1.50$. There is a fourfold degeneracy for each band. (b) Spinon spectrum for the ICSL state at $J_2/J_1 = 1.70$. The spinon bands are grouped in colors according to their separations and labeled with their total first Chern numbers. High-symmetry momenta with the subscript ℓ are defined in the reduced hexagonal Brillouin zones for $\ell \times \ell$ enlarged unit cells.

This state further breaks the lattice translation symmetries and hence differs from the CSL states discussed previously. The inhomogeneous bond expectation values result in a 2×2 enlarged unit cell as shown in Fig. 8(b). There are two types of gauge flux depending on J_2/J_1 through four hexagonal plaquettes and the total flux within the enlarged unit cell is $\phi_2 + 3\phi_2 = 2\pi/9$, half of that in the homogeneous CSL state. A similar 2×2 inhomogeneous CSL state superimposed on an average $2\pi/N$ flux per plaquette has also been reported as the lowest competing state for the antiferromagnetic SU(5) spins on the square lattice [18]. Moreover, within each hexagonal plaquette, the gauge fluxes piercing two types of the triangular plaquettes satisfy the similar relationship of the homogeneous counterpart described in Sec. IV A. Thus the ICSL state is also a variant of the Haldane model. In Fig. 9(b), the spinon band structure is plotted in the reduced Brillouin zone corresponding to a 6×6 enlarged unit cell. It is clear that the flux pattern results in a spinon band structure with 72 bands, where only the lowest eight are fully occupied, and they are separated from the others by a gap. The associated first Chern numbers for grouped bands are calculated and marked in Fig. 9(b). In spite of the inhomogeneity, the occupied spinon bands also possess the first Chern number $C_1 = \pm 1$, the same as the CSL states. Therefore, the ICSL state exhibits a total Hall conductivity $\sigma_{xy} = N/2\pi$ as well and its effective action contains the same Chern-Simons term as Eq. (20) in the continuum limit after integrating out the gapped spinons. The obtained low-energy effective theory is a topological quantum field theory with the chiral Abelian topological order and anyonic statistics. The spinon is converted into anyons with a statistical angle $\pi \pm \pi/N$ in the analogous manner of the homogeneous case. It is expected that gapless chiral states carrying spin degrees of freedom are supported by the ICSL as edge modes, and their effective theory is also described by the $\mathrm{SU}(N)_1$ WZW model.

V. DISCUSSION

In this work, we perform a mean-field analysis on the SU(N) Heisenberg model on the honeycomb lattice with both nearest- and next-nearest-neighbor antiferromagnetic interactions. In the large-N approximation, a variety of intermediate ground states are identified subject to the strict local constraints. For the SU(4) spins, the DSL state with a gauge flux π per hexagonal plaquette and its instability towards the tetramerized spin singlets when the next-nearest-neighbor exchange interaction predominates are confirmed. The putative CSL states at $J_2 = 0$ for higher SU(N) are also obtained and the associated gauge fluxes per hexagonal plaquette follow the same form of $4\pi/N$. The next-nearest-neighbor bond expectations would develop in the presence of J_2 and render the ground state to a variant of the Haldane model with $4\pi/N$ total flux through the unit cell. These CSL states preserve the lattice translation and have a unity first Chern number for the occupied spinon bands. A series of intermediate quantum phases breaking various lattice translation symmetries would appear when the next-nearest-neighbor interactions become stronger. For the SU(8) and SU(9) spins, inhomogeneous states with 2×2 ordering pattern are found. While the former preserves the time-reversal symmetry, the latter is identified as a new

ICSL state. Apart from the VCS states containing 6 sites (or 14 sites) found for the SU(6) [or the SU(7)] spins, there are two types of stripe ordered states manifesting themselves in the form of a doubled period along one of the honeycomb lattice vectors.

The SU(4) DSL state is supposed to be the ground state of the spin-orbital SU(4) symmetric Kugel-Khomskii model of Mott insulators on the honeycomb lattice. There might be an intrinsic instability due to the monopole proliferation. There is no definitive conclusion for the stability of the SU(4) DSL state at this stage. Our mean-field results provide an evidence for its stability against the antiferromagnetic next-nearest-neighbor interaction. This is also supported by the fidelity analysis using the ED method and consistent with previous variational Monte Carlo study [59]. But all numerical methods suffer the significant finite-size effect in the nearby tetramerized state, resulting in an undetermined phase boundary. The mean-field phase boundary obtained in this work is overestimated and would be modified by the $1/N$ corrections. More numerical tools such as tensor network algorithms are needed to give a conclusive result. On the other hand, multispin interaction terms, e.g., the scalar spin chirality, could destabilize the DSL state in principle. The consequence on current results is an open question.

ACKNOWLEDGMENTS

We thank Chun-Jiong Huang for useful discussions. This work is supported by the National Science Foundation of China with Grant No. 92065203, by the Ministry of Science and Technology of China with Grants No. 2018YFE0103200 and No. 2021YFA1400300, by the Shanghai Municipal Science and Technology Major Project with Grant No. 2019SHZDZX04, and by the Research Grants Council of Hong Kong with General Research Fund, Grant No. 17306520.

APPENDIX: THE SCM ALGORITHM

The SCM algorithm is a nondeterministic optimization algorithm starting from the randomly initialized auxiliary fields $\chi_{\boldsymbol{rr'}} = |\chi_{\boldsymbol{rr'}}|e^{i\varphi_{\boldsymbol{rr'}}}$ and unified chemical potentials $\mu_{\boldsymbol{r}}$ on a given geometry [19]. For convenience, both the amplitudes and phases of the bond operators $\chi_{\boldsymbol{rr'}}$ are taken to be uniform distributions, e.g., $|\chi_{\boldsymbol{rr'}}| \in [0.02, 0.20]$ and $\varphi_{\boldsymbol{rr'}} \in [0, 2\pi]$, respectively. The default value of $\mu_{\boldsymbol{r}}$ is chosen to be zero before optimization. It is obvious that the random initial state violates the desired single occupation in general and one can denote the deviation of the local fermion density as

$$\delta n_{\boldsymbol{r}} = 1 - \langle f^{\dagger}_{\boldsymbol{r}\alpha} f_{\boldsymbol{r}\alpha}\rangle, \tag{A1}$$

where the expectation value of the local density operator is obtained using the ground state of the mean-field Hamiltonian $\mathcal{H}_{\mathrm{MF}}$ with initialized parameters at this stage. To correct the density, one must adjust the chemical potential $\mu_{\boldsymbol{r}}$ locally by $\delta\mu_{\boldsymbol{r}}$. As we will show later, this adjustment will be implemented iteratively to achieve the self-consistency; therefore, it is sufficient to consider the lowest order at each step, which can be expressed as

$$\delta\mu = \mathcal{G}^{-1}\delta n. \tag{A2}$$

Here $\delta\mu$ and δn are column vectors with elements $\delta\mu_{\boldsymbol{r}}$ and $\delta n_{\boldsymbol{r}}$, respectively. The response matrix $\mathcal{G}$ is nothing but the inverse of the density-density correlation in real space and at zero frequency. It is a real symmetric matrix by definition. In principle, the correlation elements $\mathcal{G}_{\boldsymbol{rr'}}$ can be calculated from the noninteracting mean-field Hamiltonian $\mathcal{H}_{\mathrm{MF}}$. So far, all derivations are done within the framework of the standard linear response theory. However, there is a caveat that the invertibility of the density-density correlation cannot be guaranteed despite the fact that all its eigenvalues are real. Actually, at least one eigenvalue of the matrix $\mathcal{G}$ must be exactly zero because it is trivial to adjust the chemical potentials uniformly at each site. The fermion density will remain intact and result in a naive divergence of $\mathcal{G}^{-1}$. To remediate this fatal flaw, Hermele and Gurarie proposed a modified diagonalization procedure in Ref. [19]. In particular, only nonzero eigenvalues g_i are focused on after diagonalizing

$$\mathcal{G} = UgU^{-1}. \tag{A3}$$

We have assigned the index i to the diagonalized basis. In such a basis, the linear transformation in Eq. (A2) formally reduces to

$$U^{-1}\delta\mu = g^{-1}U^{-1}\delta n. \tag{A4}$$

By mapping the vanishing eigenvalues to infinity, the adjustment of the chemical potential $\delta\mu$ becomes well defined; that is,

$$(U^{-1}\delta\mu)_i = \begin{cases} g_i^{-1}U^{-1}\delta n, & g_i \neq 0 \\ 0, & g_i = 0. \end{cases} \tag{A5}$$

With the above relationship, a new mean-field Hamiltonian $\mathcal{H}_{\mathrm{MF}}$ and related ground state can be generated by a simple replacement, $\mu_{\boldsymbol{r}} \to \mu_{\boldsymbol{r}} + \delta\mu_{\boldsymbol{r}}$. The local fermion density $\delta n_{\boldsymbol{r}}$ should be updated concurrently, resulting in a new deviation $\delta n_{\boldsymbol{r}}$ as Eq. (A1). Then, the problem returns to find the adjustment of chemical potentials in the current ground state. These processes complete the self-consistent procedure. The problem of searching for an appropriate set of chemical potential deviation $\delta\mu_{\boldsymbol{r}}$ can be solved by iterating the procedure until a fixed point is reached. This is the core of the SCM algorithm to strictly impose the local constraints $n_{\boldsymbol{r}} = \langle f^{\dagger}_{\boldsymbol{r}\alpha} f_{\boldsymbol{r}\alpha}\rangle = 1$.

After meeting the first saddle-point condition, Eq. (5), the others about the bound operators still need to be satisfied. With the modified chemical potentials calculated in the previous stage, an updated set of auxiliary fields $\chi_{\boldsymbol{rr'}}$ can be determined via

$$\chi_{\langle \boldsymbol{rr'}\rangle} \to -\langle f^{\dagger}_{\boldsymbol{r'}\alpha} f_{\boldsymbol{r}\alpha}\rangle/N, \tag{A6}$$

$$\chi_{\langle\langle \boldsymbol{r},\boldsymbol{r'}\rangle\rangle} \to -J_2/J_1\langle f^{\dagger}_{\boldsymbol{r'}\alpha} f_{\boldsymbol{r}\alpha}\rangle/N. \tag{A7}$$

Once again, the local constraints are violated if the system has not yet converged to the true saddle point. The amended auxiliary fields, together with the chemical potentials satisfying the single occupation condition in the previous stage, can be treated as a new and better starting point. The two-stage updating procedure is thus implemented iteratively until

reaching a convergence in energy within a given numerical error. It has been proved rigorously in Ref. [19] that within each optimization process the energy of the final state must be less than or equal to that of the initial state. Therefore, the SCM algorithm ends at one of the local energy minima. In order to best estimate the global minimum, the program should be run with differently initialized fields, which can be realized by varying the random number seeds. Finally, a collection of local minima will be reaped and the lowest one is accepted as the best result of the ground state.

[1] S. Sachdev and N. Read, Large N expansion for frustrated and doped quantum antiferromagnets, Int. J. Mod. Phys. B **05**, 219 (1991).

[2] B. Coqblin and J. R. Schrieffer, Exchange interaction in alloys with cerium impurities, Phys. Rev. **185**, 847 (1969).

[3] A. Auerbach, *Interacting Electrons and Quantum Magnetism* (Springer-Verlag, New York, 1994).

[4] A. V. Gorshkov, M. Hermele, V. Gurarie, C. Xu, P. S. Julienne, J. Ye, P. Zoller, E. Demler, M. D. Lukin, and A. M. Rey, Two-orbital SU(N) magnetism with ultracold alkaline-earth atoms, Nat. Phys. **6**, 289 (2010).

[5] S. Taie, R. Yamazaki, S. Sugawa, and Y. Takahashi, An SU(6) Mott insulator of an atomic Fermi gas realized by large-spin Pomeranchuk cooling, Nat. Phys. **8**, 825 (2012).

[6] C. Wu, J.-P. Hu, and S.-C. Zhang, Exact SO(5) Symmetry in the Spin-3/2 Fermionic System, Phys. Rev. Lett. **91**, 186402 (2003).

[7] C. Wu, Competing Orders in One-Dimensional Spin-3/2 Fermionic Systems, Phys. Rev. Lett. **95**, 266404 (2005).

[8] D. Wang, Y. Li, Z. Cai, Z. Zhou, Y. Wang, and C. Wu, Competing Orders in the 2D Half-Filled SU(2N) Hubbard Model through the Pinning-Field Quantum Monte Carlo Simulations, Phys. Rev. Lett. **112**, 156403 (2014).

[9] F. Scazza, C. Hofrichter, M. Höfer, P. C. D. Groot, I. Bloch, and S. Fölling, Observation of two-orbital spin-exchange interactions with ultracold SU(N)-symmetric fermions, Nat. Phys. **10**, 779 (2014).

[10] C. Hofrichter, L. Riegger, F. Scazza, M. Höfer, D. R. Fernandes, I. Bloch, and S. Fölling, Direct Probing of the Mott Crossover in the SU(N) Fermi-Hubbard Model, Phys. Rev. X **6**, 021030 (2016).

[11] B. Song, Y. Yan, C. He, Z. Ren, Q. Zhou, and G.-B. Jo, Evidence for Bosonization in a Three-Dimensional Gas of SU(N) Fermions, Phys. Rev. X **10**, 041053 (2020).

[12] H. Ozawa, S. Taie, Y. Takasu, and Y. Takahashi, Antiferromagnetic Spin Correlation of SU($\mathcal{N}$) Fermi Gas in an Optical Superlattice, Phys. Rev. Lett. **121**, 225303 (2018).

[13] S. Taie, E. Ibarra-García-Padilla, N. Nishizawa, Y. Takasu, Y. Kuno, H.-T. Wei, R. T. Scalettar, K. R. A. Hazzard, and Y. Takahashi, Observation of antiferromagnetic correlations in an ultracold SU(N) Hubbard model, arXiv:2010.07730.

[14] A. Goban, R. B. Hutson, G. E. Marti, S. L. Campbell, M. A. Perlin, P. S. Julienne, J. P. D'Incao, A. M. Rey, and J. Ye, Emergence of multi-body interactions in a fermionic lattice clock, Nature (London) **563**, 369 (2018).

[15] C. Xu and L. Balents, Topological Superconductivity in Twisted Multilayer Graphene, Phys. Rev. Lett. **121**, 087001 (2018).

[16] Y.-H. Zhang and A. Vishwanath, Electrical detection of spin liquids in double moiré layers, arXiv:2005.12925.

[17] Y.-H. Zhang, D. N. Sheng, and A. Vishwanath, SU(4) Chiral Spin Liquid, Exciton Supersolid, and Electric Detection in Moiré Bilayers, Phys. Rev. Lett. **127**, 247701 (2021).

[18] M. Hermele, V. Gurarie, and A. M. Rey, Mott Insulators of Ultracold Fermionic Alkaline Earth Atoms: Underconstrained Magnetism and Chiral Spin Liquid, Phys. Rev. Lett. **103**, 135301 (2009).

[19] M. Hermele and V. Gurarie, Topological liquids and valence cluster states in two-dimensional SU(N) magnets, Phys. Rev. B **84**, 174441 (2011).

[20] X.-P. Yao, Y. Gao, and G. Chen, Topological chiral spin liquids and competing states in triangular lattice SU(N) Mott insulators, Phys. Rev. Research **3**, 023138 (2021).

[21] J.-Y. Chen, J.-W. Li, P. Nataf, S. Capponi, M. Mambrini, K. Totsuka, H.-H. Tu, A. Weichselbaum, J. von Delft, and D. Poilblanc, Abelian SU(N)$_1$ chiral spin liquids on the square lattice, Phys. Rev. B **104**, 235104 (2021).

[22] S. R. Manmana, K. R. A. Hazzard, G. Chen, A. E. Feiguin, and A. M. Rey, SU(N) magnetism in chains of ultracold alkaline-earth-metal atoms: Mott transitions and quantum correlations, Phys. Rev. A **84**, 043601 (2011).

[23] G. Chen, K. R. A. Hazzard, A. M. Rey, and M. Hermele, Synthetic-gauge-field stabilization of the chiral-spin-liquid phase, Phys. Rev. A **93**, 061601(R) (2016).

[24] F. F. Assaad, Phase diagram of the half-filled two-dimensional SU(N) Hubbard-Heisenberg model: A quantum Monte Carlo study, Phys. Rev. B **71**, 075103 (2005).

[25] F. L. Buessen, D. Roscher, S. Diehl, and S. Trebst, Functional renormalization group approach to SU(N) Heisenberg models: Real-space renormalization group at arbitrary N, Phys. Rev. B **97**, 064415 (2018).

[26] D. Roscher, F. L. Buessen, M. M. Scherer, S. Trebst, and S. Diehl, Functional renormalization group approach to SU(N) Heisenberg models: Momentum-space renormalization group for the large-N limit, Phys. Rev. B **97**, 064416 (2018).

[27] F. H. Kim, K. Penc, P. Nataf, and F. Mila, Linear flavor-wave theory for fully antisymmetric SU(N) irreducible representations, Phys. Rev. B **96**, 205142 (2017).

[28] W. M. H. Natori, R. Nutakki, R. G. Pereira, and E. C. Andrade, SU(4) Heisenberg model on the honeycomb lattice with exchange-frustrated perturbations: Implications for twistronics and Mott insulators, Phys. Rev. B **100**, 205131 (2019).

[29] M. G. Yamada, M. Oshikawa, and G. Jackeli, Emergent SU(4) Symmetry in α-$ZrCl_3$ and Crystalline Spin-Orbital Liquids, Phys. Rev. Lett. **121**, 097201 (2018).

[30] M. G. Yamada, M. Oshikawa, and G. Jackeli, SU(4)-symmetric quantum spin-orbital liquids on various lattices, arXiv:2103.17076.

[31] H. H. Zhao, C. Xu, Q. N. Chen, Z. C. Wei, M. P. Qin, G. M. Zhang, and T. Xiang, Plaquette order and deconfined quantum critical point in the spin-1 bilinear-biquadratic Heisenberg model on the honeycomb lattice, Phys. Rev. B **85**, 134416 (2012).

[32] P. Corboz, M. Lajkó, K. Penc, F. Mila, and A. M. Läuchli, Competing states in the SU(3) Heisenberg model on the honeycomb lattice: Plaquette valence-bond crystal versus dimerized color-ordered state, Phys. Rev. B **87**, 195113 (2013).

[33] S. S. Chung and P. Corboz, SU(3) fermions on the honeycomb lattice at $\frac{1}{3}$ filling, Phys. Rev. B **100**, 035134 (2019).

[34] P. Corboz, M. Lajkó, A. M. Läuchli, K. Penc, and F. Mila, Spin-Orbital Quantum Liquid on the Honeycomb Lattice, Phys. Rev. X **2**, 041013 (2012).

[35] G. Szirmai, E. Szirmai, A. Zamora, and M. Lewenstein, Gauge fields emerging from time-reversal symmetry breaking for spin-5/2 fermions in a honeycomb lattice, Phys. Rev. A **84**, 011611(R) (2011).

[36] P. Sinkovicz, A. Zamora, E. Szirmai, M. Lewenstein, and G. Szirmai, Spin liquid phases of alkaline-earth-metal atoms at finite temperature, Phys. Rev. A **88**, 043619 (2013).

[37] P. Nataf, M. Lajkó, P. Corboz, A. M. Läuchli, K. Penc, and F. Mila, Plaquette order in the SU(6) Heisenberg model on the honeycomb lattice, Phys. Rev. B **93**, 201113(R) (2016).

[38] L. Balents, Spin liquids in frustrated magnets, Nature (London) **464**, 199 (2010).

[39] A. Mulder, R. Ganesh, L. Capriotti, and A. Paramekanti, Spiral order by disorder and lattice nematic order in a frustrated Heisenberg antiferromagnet on the honeycomb lattice, Phys. Rev. B **81**, 214419 (2010).

[40] X.-P. Yao, J. Q. Liu, C.-J. Huang, X. Wang, and G. Chen, Generic spiral spin liquids, Front. Phys. **16**, 53303 (2021).

[41] R. Ganesh, J. van den Brink, and S. Nishimoto, Deconfined Criticality in the Frustrated Heisenberg Honeycomb Antiferromagnet, Phys. Rev. Lett. **110**, 127203 (2013).

[42] B. K. Clark, D. A. Abanin, and S. L. Sondhi, Nature of the Spin Liquid State of the Hubbard Model on a Honeycomb Lattice, Phys. Rev. Lett. **107**, 087204 (2011).

[43] S.-S. Gong, D. N. Sheng, O. I. Motrunich, and M. P. A. Fisher, Phase diagram of the spin-$\frac{1}{2}$ J_1-J_2 Heisenberg model on a honeycomb lattice, Phys. Rev. B **88**, 165138 (2013).

[44] S.-S. Gong, W. Zhu, and D. N. Sheng, Quantum phase diagram of the spin-1 J_1-J_2 Heisenberg model on the honeycomb lattice, Phys. Rev. B **92**, 195110 (2015).

[45] P. H. Y. Li and R. F. Bishop, Ground-state phases of the spin-1 J_1-J_2 Heisenberg antiferromagnet on the honeycomb lattice, Phys. Rev. B **93**, 214438 (2016).

[46] M. Hermele, T. Senthil, M. P. A. Fisher, P. A. Lee, N. Nagaosa, and X.-G. Wen, Stability of $U(1)$ spin liquids in two dimensions, Phys. Rev. B **70**, 214437 (2004).

[47] T. Grover, Entanglement Monotonicity and the Stability of Gauge Theories in Three Spacetime Dimensions, Phys. Rev. Lett. **112**, 151601 (2014).

[48] V. Calvera and C. Wang, Theory of Dirac spin-orbital liquids: Monopoles, anomalies, and applications to $SU(4)$ honeycomb models, arXiv:2103.13405.

[49] X.-Y. Song, C. Wang, A. Vishwanath, and Y.-C. He, Unifying description of competing orders in two-dimensional quantum magnets, Nat. Commun. **10**, 4254 (2019).

[50] S.-S. Gong, W. Zheng, M. Lee, Y.-M. Lu, and D. N. Sheng, Chiral spin liquid with spinon Fermi surfaces in the spin-$\frac{1}{2}$ triangular Heisenberg model, Phys. Rev. B **100**, 241111(R) (2019).

[51] É. Dupuis, R. Boyack, and W. Witczak-Krempa, Anomalous dimensions of monopole operators at the transitions between Dirac and topological spin liquids, arXiv:2108.05922.

[52] Q. Zhang and T. Li, Bosonic resonating valence bond theory of the possible chiral spin-liquid state in the triangular-lattice Hubbard model, Phys. Rev. B **104**, 075103 (2021).

[53] Y. Iqbal, F. Ferrari, A. Chauhan, A. Parola, D. Poilblanc, and F. Becca, Gutzwiller-projected states for the J_1-J_2 Heisenberg model on the kagome lattice: Achievements and pitfalls, Phys. Rev. B **104**, 144406 (2021).

[54] A. Keselman, B. Bauer, C. Xu, and C.-M. Jian, Emergent Fermi Surface in a Triangular-Lattice SU(4) Quantum Antiferromagnet, Phys. Rev. Lett. **125**, 117202 (2020).

[55] A. Keselman, L. Savary, and L. Balents, Dimer description of the SU(4) antiferromagnet on the triangular lattice, SciPost Phys. **8**, 76 (2020).

[56] H.-K. Jin, R.-Y. Sun, H.-H. Tu, and Y. Zhou, A unified theory for the SU(4) spin-orbital model on the triangular lattice, arXiv:2106.09318.

[57] B. Bauer, P. Corboz, A. M. Läuchli, L. Messio, K. Penc, M. Troyer, and F. Mila, Three-sublattice order in the SU(3) Heisenberg model on the square and triangular lattice, Phys. Rev. B **85**, 125116 (2012).

[58] Y. Iqbal, W.-J. Hu, R. Thomale, D. Poilblanc, and F. Becca, Spin liquid nature in the Heisenberg J_1-J_2 triangular antiferromagnet, Phys. Rev. B **93**, 144411 (2016).

[59] M. Lajkó and K. Penc, Tetramerization in a SU(4) Heisenberg model on the honeycomb lattice, Phys. Rev. B **87**, 224428 (2013).

[60] M. Kawamura, K. Yoshimi, T. Misawa, Y. Yamaji, S. Todo, and N. Kawashima, Quantum lattice model solver $\mathcal{H}\Phi$, Comput. Phys. Commun. **217**, 180 (2017).

[61] S. Yang, K. Sun, and S. Das Sarma, Quantum phases of disordered flatband lattice fractional quantum Hall systems, Phys. Rev. B **85**, 205124 (2012).

[62] F. D. M. Haldane, Model for a Quantum Hall Effect without Landau Levels: Condensed-Matter Realization of the "Parity Anomaly," Phys. Rev. Lett. **61**, 2015 (1988).

[63] M. Nakahara, *Geometry, Topology and Physics*, 2nd ed. (CRC Press, Boca Raton, FL, 2018).